Chin.J.Geochem.(2014)33:325–335
DOI: 10.1007/s11631-014-0695-x

Geochemistry of mafic rocks and melt inclusions and their implications for the heat source of the 14.0°S hydrothermal field, South Mid-Atlantic Ridge

LI Bing[1], SHI Xuefa[1*], YANG Yaomin[2], YE Jun[1], GAO Jingjing[1], and ZHENG Wenqin[3]

[1] *Key Laboratory of Marine Sedimentology and Environmental Geology, First Institute of Oceanography, State Oceanic Administration, Qingdao 266061, China*

[2] *National Deep Sea Center, State Oceanic Administration, Qingdao 266061, China*

[3] *Institute of Geochemistry, Chinese Academy of Sciences, Guiyang 550002, China*

[*] *Corresponding author, E-mail: xfshi@fio.org.cn; bli@fio.org.cn*

Received November 1, 2013; accepted January 21, 2014

Abstract Fresh rocks sampled from the 14.0°S hydrothermal field of the South Atlantic Ridge can be divided into two categories: olivine-gabbro and basalt. The olivine-gabbro is composed mainly of three types of minerals: olivine, clinopyroxene and plagioclase, while a multitude of melt inclusions occur in the plagioclase phenocrysts of the basalts. We analyzed the whole-rock, major and trace elements contents of the basalts, the mineral chemistry of phenocrysts and melt inclusions in the basalts, and the mineral chemistry of olivine-clinopyroxene-plagioclase in the olivine-gabbro, then simulated magma evolution within the crust using the COMAGMAT program. The whole-rock geochemistry shows that all the basalts exhibit typical N-MORB characteristics. In addition, the mineral chemistry characteristics of the olivine-gabbro (low-Fo olivine, low-Mg# clinopyroxene, high-TiO_2 clinopyroxene, low-An plagioclase), show that strong magma differentiation occurred within the crust. Nevertheless, significant discrepancies between those minerals and phenocrysts in the basalts (high-Fo olivine, high-An plagioclase) reflect the heterogeneity of magma differentiation. High Mg# (≈0.72) melt inclusions isobaric partial crystallization simulations suggest that the magma differentiation occurred at the depth shallower than 13.03 km below the seafloor, and both the vertical differentiation column shows distinct discrepancies from that of a steady-state magma chamber. Instead, a series of independent magma intrusions probably occurred within the crust, and their corresponding crystallized bodies, as the primary high-temperature thermal anomalies within the off-axis crust, probably act as the heat source for the development of the 14.0°S hydrothermal system.

Key words 14.0°S hydrothermal field; mineral geochemistry; olivine-gabbro; melt inclusion; magma intrusion

1 Introduction

Hydrothermal activities and associated mineralization systems at the mid-ocean ridges are strongly constrained by magmatism, as those systems are generally driven by magma-related intra-crust bodies (Fouquet, 1997; Hannington et al., 2005). However, the intensity of magmatism is largely dependent on the ridge spreading rate, with different spreading ridges demonstrating significantly different spatial distributions and scales of magmatic activities (Wilcock and Delaney, 1996; Baker, 2009; Lowell, 2010). At fast spreading ridges (e.g. EPR-East Pacific Rise), magma chambers formed by primary magma mixing are widely developed within the oceanic crust, which are characterized by steady-state shallow locations, nearly 1.0–2.0 km below the seafloor (Bach and Früh, 2010). The seawater thus readily penetrated downwards along shallow fractures to zones near the magma chamber, then was heated and flew upwards to form hydrothermal sulfide deposits (Alt, 1995; Tivey, 2007; Coumou et al., 2008; Wilcock et al., 2009). However, at those magma-robust ridges, the established hydrothermal mineralization system tends to be easily destroyed by frequent magma events (diking and eruption), resulting in the low probability of the develop-

ment of large massive sulfide deposits. On the other hand, slow spreading ridges (e.g. MAR-Middle Atlantic Ridge), which are characterized by relatively weak magmatism, generally lack steady-state magma chambers for their relatively low mantle temperature (Niu and O'hara, 2008), and consequently have a low degree of mantle partial melting. Instead, several small-scale magma intrusions commonly occurred within the crust (Mccaig and Harris, 2012). The lack of a steady-state magma chamber makes it difficult to form corresponding hydrothermal systems. However, once a hydrothermal system was formed in this setting, it would not be as easily damaged by frequent magma events as those at the fast spreading ridges, and the established stable hydrothermal system is likely to exist for a long period, thus leading to the development of large hydrothermal sulfide deposits (Fouquet, 1997). Nevertheless, although slow spreading ridges are poor in magma, they generally show strong magmatic heterogeneity along the ridge axis (Haase, 2009). Given the crucial role of complex magmatism in hydrothermal sulfide formation (German, 2004), it is essential to perform further investigations into ridge crust magmatism in order to determine the possibility of the existence of large sulfide deposits for certain ridge segments.

The 14.0°S hydrothermal field was first discovered in 2009 during the Chinese R/V Dayang Yihao Cruise 21 (Tao et al., 2011), and is located on the inside corner of the intersection of the southern Mid-Atlantic Ridge and the Cardno transform fault. This field is characterized by high temperature and an abundance of high-temperature sulfide minerals (pyrite and chalcopyrite) on the associated deposits. Unlike other inside corners, which are composed mainly of ultramafic blocks, the 14.0°S hydrothermal field is mafic, suggesting the critical effect of magmatism on its development. Four other hydrothermal systems were identified previously on the ridge inside corners: (1) the Lost City (Von Damm, 2001; Kelley and Karson, 2001; Früh-Green et al., 2003), (2) the MenezHom (Charlou et al., 1997), (3) the Saldanha field (Dias et al., 2011), and (4) the 12°50′N field (Dekov et al., 2011).These systems were found in the settings composed mainly of ultramafic rocks, which have a substantial impact on the hydrothermal heat supply, and the absence of magmatism results in the low-temperature properties of these fields. The 14.0°S field is the first hydrothermal field discovered at the ridge-transform inside-corner intersection in the South Atlantic, and the first mafic-host inside-corner intersection high-temperature hydrothermal field. Determining the characteristics of its heat source would be of great significance for further studying hydrothermal mineralization. In this paper, we first examined the whole-rock geochemistry, mineral geochemistry, and melt inclusion geochemistry of fresh basalt and gabbro, then analyzed the characteristics of magmatic activities in this region and discussed their corresponding effects on the related hydrothermal systems. All these efforts are of great significance to elucidate the hydrothermal mineralization processes in this area and the hydrothermal ore-forming environment at this magmatic inside-corner high.

2 Geological setting

The South Mid-Atlantic Ridge (SMAR) system begins at the Romanche gap near the equator, and extends southwards to the Bouvet triple junction (54°S). As a typical slow spreading ridge, its full spreading rate is 2–5 cm/a (Dick et al., 2003; Devey et al., 2010). The magmatism is generally weak, and the discontinuous volcanic zones typically occur in the internal central valleys (Macdonald et al., 1991). The SMAR is interrupted by the right-handed Cardno fracture zone near 14.0°S, where two high lands occur at the insider-corner intersection (Fig. 1): one rough massif is close to the west rift valley, and the other dome-like massif occurs adjacent to the right side of the rough massif. The rough massif is magmatic in origin, and its western slope is just located in the east of the rift valley wall. Although there is a lack of sampling from the dome-like massif, the seafloor morphology there presents a moderately smooth relief and a series of parallel corrugations on its surface, which means it is probably a fossil megamullion. Inside-corner highs commonly occur along slow spreading mid-ocean ridges at rifted spreading centers, within transform fault intersection zones. Several mechanisms have been proposed to explain the origin and development of the inside-corner highs; however, the question remains controversial (Tucholke and Lin, 1994; Chen and Lin, 1999).

Our investigations revealed that on the western slope of the volcanic dome at this inside-corner high, there are at least two active off-axis hydrothermal sites and associated hydrothermal products, including silica-rich sulfides and their red oxides, and other hydrothermal siliceous products. The gap of the two sites is less than 1 km, and its distance from the spreading center is approximately 5 km, but the difference in water depth is so large as to exceed 1 km, with the shallower hydrothermal site at a water depth of -1943 m, and the deeper one at a water depth of -2840 m. Except for the extensive basalts, intrusive rocks such as diabase and gabbro are also situated on the dome. Many fissure structures occur on the volcanic inside-corner highs, and pelagic sediments of varying thicknesses cover a large area of the dome. Such observations to some extent reflect that magmatism in this area is not active in recent years.

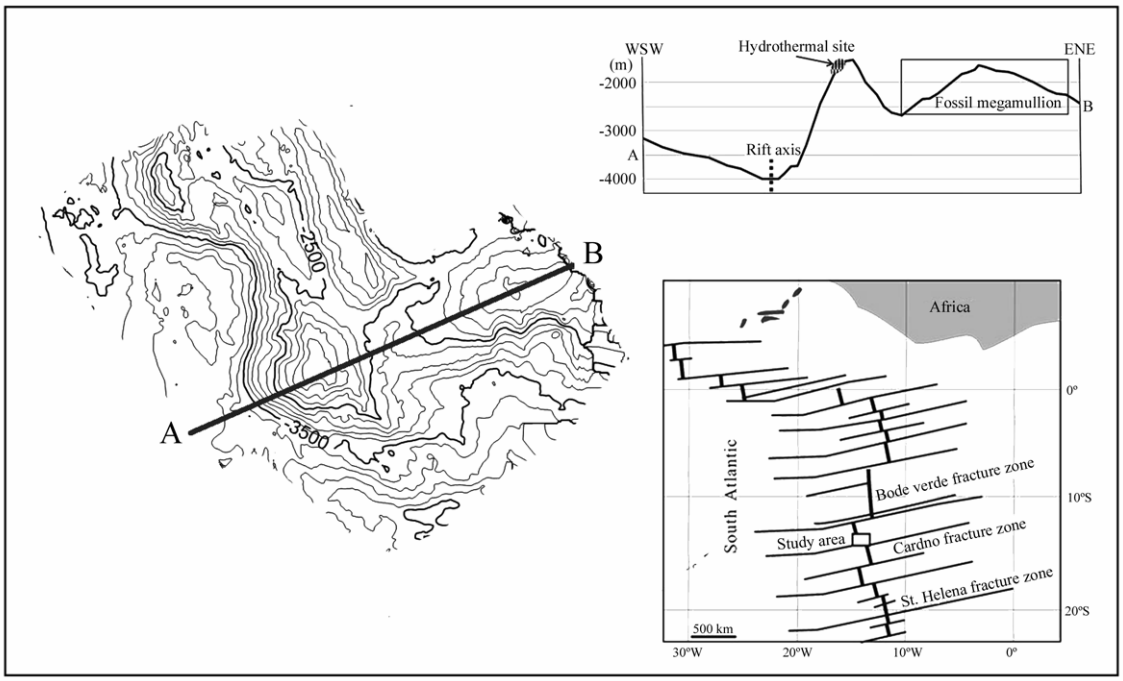

Fig. 1. Sketch map showing the location of the 14.0°S hydrothermal field between the South Mid-Atlantic Ridge and the Cardno fracture zone.

3 Materials and methods

The studied samples are all mafic rocks, which were collected from the surface of the volcanic dome by the TV-Grabs and Remote Operated Vehicle (ROV). In order to eliminate the effect of supergene alteration, our research focused only on fresh rocks: fresh basalts and fresh olivine-gabbro. Typical photos (both hand specimens and their corresponding thin-section photomicrographs) are shown in Fig. 2. Some plagioclase phenocrysts of large crystal sizes (generally larger than 1 mm) occurred in the basalts (Fig. 2C). Moreover, a multitude of melt inclusions occurred in several of those plagioclase phenocrysts (Fig. 2D). The olivine-gabbro consists of three types of minerals: plagioclase, olivine, and clinopyroxene (especially plagioclase) that commonly show holocrystalline texture with grain sizes ranging from several hundred microns to several millimeters.

The major and trace elements contents of the bulk rock samples were determined by inductively coupled plasma-optical emission spectroscopy (ICP-AES, iCAP6300, Thermo Fisher) and inductively coupled plasma mass spectrometry (ICP-MS, X Series 2, Thermo Fisher), respectively. In order to guarantee the reliability of the results, we selected 10% of the samples randomly for repeated analysis, and made it sure that the relative errors and relative standard deviations for all the elements were less than 5%. This work was conducted at the First Institute of Oceanography, State Oceanic Administration (SOA). Mineral chemistry analysis was conducted on an EPMA-1600 electron probe at the State Key Laboratory of Ore Deposit Geochemistry, Institute of Geochemistry, Chinese Academy of Sciences, under the following working conditions: the acceleration voltage was 25 kV, the acceleration electric current was $2e^{-8}$, the electron beam diameter was 5–10 μm, with SPI international standards and an absolute error less than 0.1 wt%.

4 Results

4.1 Major and trace elements in basalts

The major and trace elements concentrations of the 10 basalt samples are given in Table 1. For major elements, the samples are all characterized by low MgO contents (MgO=6.0 wt%–7.2 wt%), reflecting that the erupted magma in this area had highly evolved within the crust. In addition, two of the residual glass samples has a SiO_2 content of up to 54.1 wt%, and the others have the equivalent values ranging from 49.4 wt% to 51.8 wt%. The relatively high SiO_2 contents of the basalts also indicate a high degree of magma evolution. The contents of other oxides in the samples: CaO:10.5 wt%–11.6 wt%, Al_2O_3: 12.7 wt%–15.1 wt%, $Na_2O+K_2O<5.0$ wt%. All those oxide parameters show that the basalts are in line with the characteristics of N-MORB. Compared with the primary N-MORB (Presnall and Hoove, 1987), those basalts are characterized by relatively high SiO_2 and low MgO contents, suggesting magmatic differentiation within the crust.

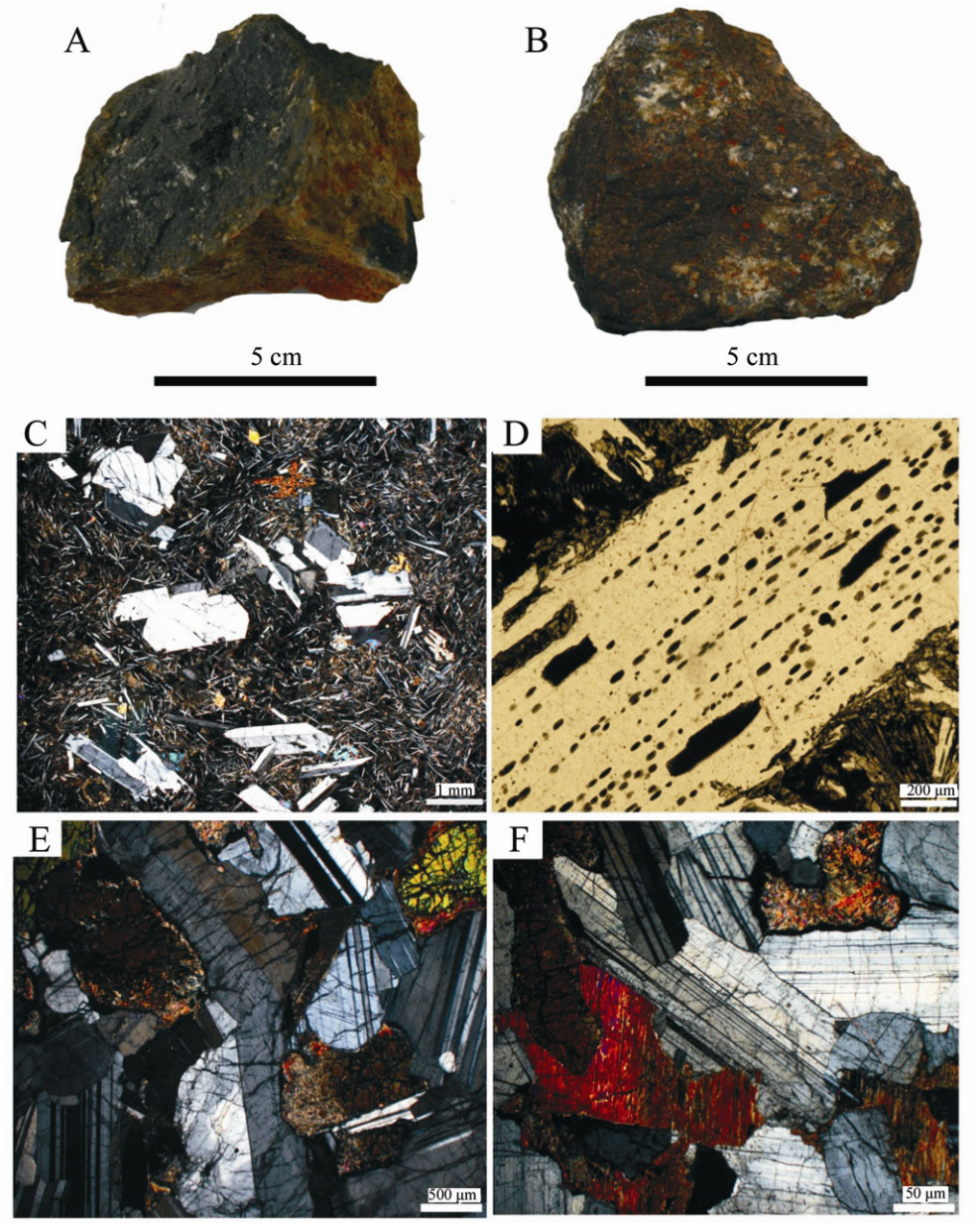

Fig. 2. Rock hand specimens with corresponding thin-section photomicrographs. A. Basalt, hand specimen, massive structure, no obvious alteration. Plagioclase phenocrysts are visible to the naked eye; B. olivine-gabbro, hand specimen, massive structure, no obvious alteration, and large mineral grains with holocrystalline texture; C. tholeiite, thin-section photomicrograph (crossed nicol), porphyritic-like texture, large plagioclase with a handful of dark mineral phenocrysts (olivine and clinopyroxene) can be identified, large amounts of plagioclase microcrystallines can be identified as well (crossed nicol); D. a multitude of melt inclusions distributed along the plagioclase cleavages in the plagioclase phenocrysts as shown in C (parallel nicols); E. olivine-gabbro, thin-section photomicrograph, and huge mineral crystals (megacrysts). Olivine was surrounded by plagioclase while plagioclase has been “bitten” by olivine (crossed nicol); F. olivine-gabbro, thin-section photomicrograph, clinopyroxene appears in the plagioclase clearance, "eating" their surrounding plagioclase (crossed nicol).

For trace elements, the large ion lithophile elements (LILE) show more losses than the high field strength elements (HFSE), which meets the standards of N-MORB. However, the contents of not only the large ion lithophile elements Ba, La, Pr, Nb, and Sr, but also the high field strength elements Zr, Hf, and Ce, are generally lower than those in the average N-MORB (Niu and O’hara, 2003), which means the partially melted mantle at 14.0°S is a more depleted one. Differences in trace element contents among samples may be due to different degrees of magma fractional crystallization. Besides, the Ta contents of

each sample show an obvious positive anomaly, leading to significantly lower Nb/Ta ratios than those in the average N-MORB (Niu and O'hara, 2003). Nevertheless, Nb and Ta always have similar geochemical characteristics, therefore fractional distillation is unlikely to happen to them, and their distillation there may lead us to take the clinopyroxene crystallization into consideration, as Nb is more incompatible than Ta, and the crystallization of clinopyroxene within the crust would undoubtedly result in the elevation of Ta in residual magma.

A spider diagram of primitive mantle-normalized trace elements, as well as the chondrite-normalized REE patterns of basalts, are shown in Fig. 3. Most of them exhibit typical "left-leaning" distribution patterns, indicating a strong loss of incompatible elements. Only one sample did not exhibit this feature; this glass represent the most highly evolved magma composition, and their "flattened" patterns to some extent reflect the enrichment of incompatible elements in the residual magma.

4.2 Mineral geochemistry of olivine-clinopyroxene-plagioclase

Results of electron microprobe analysis and related parameters for plagioclase and olive phenocrysts in the basalts, as well as olivine, clinopyroxene, and plagioclase in the olivine-gabbro are given in Tables 2, 3 and 4. The Fo values of olivine in the basalts (82.74–83.42) is significantly different from that of olivine-gabbro (75.74–77.73). For the two groups of olivine, the Mg# for their corresponding balanced magma {Mg#(melt)=1/[(1/Fo-1)/(Kd+1)]}, Kd=0.33) (Roeder and Emslie, 1970) are within the ranges of 0.64–0.67 (olivine in basalts) and 0.42–0.46 (olivine in olivine-gabbro), respectively. The olivine-balanced magma temperature can be calculated using Mg#(melt) as follows: [Tliqudus(℃)=1066+12.067 *Mg#+312.3*$(Mg\#)^2$]. The results show that the temperature of magma in balance with olivine in the basalts (1200.67–1213.97℃) is significantly different (nearly 70℃) from that in the olivine-gabbro (1124.83–1138.92℃).

Clinopyroxene has similar augitic composition in the olivine-gabbro samples (Fig. 4), but is close to the diopside-augite boundary. The Mg# values of clinopyroxene in the olivine-gabbro samples vary from 80.53 to 82.64 (Table 3). Clinopyoxene compositions show constant CaO contents, with Al_2O_3 contents varying between those of the high-Mg# and low-Mg# clinopyroxene (Stone and Niu, 2009), and Cr_2O_3 contents varying from 0.17 wt% to 0.10 wt%, far below the Cr_2O_3 contents of the high-Mg# clionopyroxene (1.0 wt%–1.5 wt%), but similar to those of the low-Mg# clinopyroxene (Stone and Niu, 2009). High TiO_2 contents in clinopyroxene are 0.87 wt%–1.47 wt%, showing a negative relationship with Mg#.

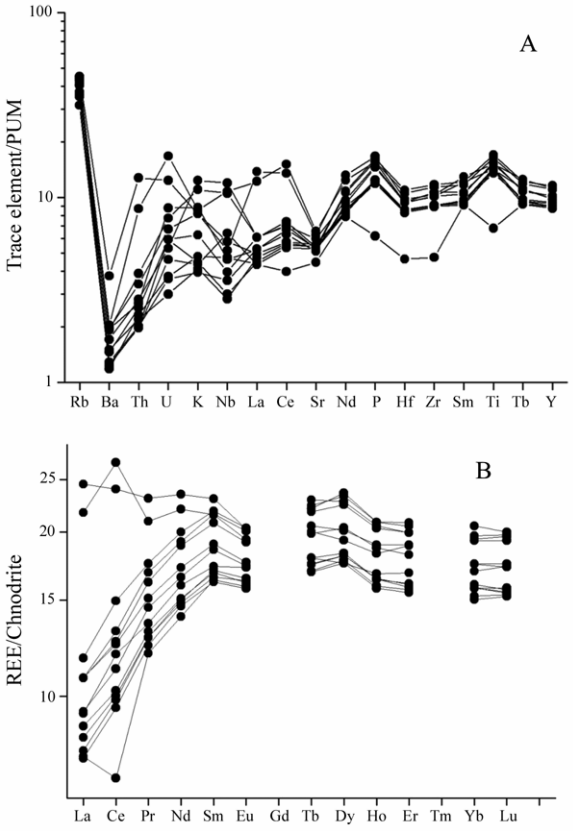

Fig. 3. A. The spider diagram of primitive mantle-normalized trace elements in the basalts; B. chondrite-normalized REE patterns of the basalts.

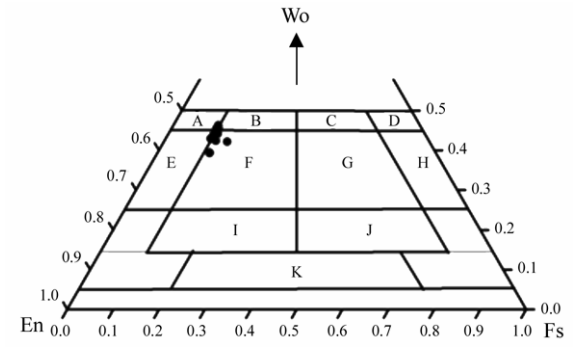

Fig. 4. The Wo-En-Fs classification graph for pyroxenes (Morimoto, 1988). A. Diopside; B. sub-diopside; C. iron sub-diopside; D. hedenbergite; E. endiopside; F. augite; G. iron augite; H. iron hedenbergite; I. calcium-poor augite; J. calcium-iron-poor augite; K. pigeonite.

Table 1 Major-and trace elements compositions of the basalt samples

Station	ROVs-02	ROVs-02	ROVs-01	ROVs-01	TV-grabs-3	TV-grabs-3	TV-grabs-3	TV-grabs-10	TV-grabs-10	TV-grabs-10	
Sample	ROV 02-R1	ROV 02-R2	ROV 01-R1	ROV 01-R2	TVG 03-R1	TVG 03-R2	TVG 03-R3	TVG 10-R1	TVG 10-R2	TVG 10-R3	Average N-MORB[a]
CaO	10.85	11.59	11.07	10.54	10.78	11.36	10.76	10.52	11.30	11.23	-
Al_2O_3	15.13	13.70	13.05	14.02	14.33	14.29	14.20	12.68	13.21	13.64	-
Fe_2O_3	10.44	11.20	11.60	11.64	11.37	11.15	11.28	10.26	9.22	10.60	-
MgO	6.48	5.96	6.24	6.11	6.17	6.29	6.20	7.00	7.20	7.00	-
SiO_2	49.36	51.73	51.02	51.70	51.55	51.06	51.73	54.11	54.08	51.79	-
Na_2O	2.63	2.68	2.93	2.64	2.51	2.67	2.58	2.39	2.01	2.66	-
MnO_2	0.19	0.14	0.18	0.14	0.15	0.14	0.25	0.13	0.13	0.13	-
K_2O(%)	0.17	0.15	0.11	0.22	0.19	0.07	0.14	0.07	0.09	0.08	-
P_2O_5(%)	0.11	0.04	0.15	0.05	0.05	0.05	0.05	0.04	0.06	0.04	-
TiO_2(%)	1.34	0.84	1.66	0.93	0.86	0.90	0.82	0.79	0.71	0.82	-
Th($\times10^{-6}$)	0.17	0.22	0.16	0.18	0.25	0.13	0.82	0.14	0.15	0.13	0.2
Nb($\times10^{-6}$)	2.59	3.23	2.22	6.71	5.90	1.99	2.90	1.58	2.66	1.68	3.33
Rb($\times10^{-6}$)	4.28	23.79	23.23	22.32	4.5	19.31	24.81	19.98	17.37	20.49	1.32
Ba($\times10^{-6}$)	6.95	9.98	7.44	8.69	16.76	6.56	19.21	7.67	6.03	6.32	13.41
U($\times10^{-6}$)	0.16	0.12	0.11	0.1	0.14	0.07	0.22	0.05	0.07	0.11	0.08
La($\times10^{-6}$)	2.88	2.73	3.35	3.35	3.35	2.90	7.60	2.60	2.40	2.46	4.13
Ce($\times10^{-6}$)	9.65	8.27	10.64	10.19	10.06	9.07	19.40	8.09	5.71	7.95	12.9
Sr($\times10^{-6}$)	94.48	98.9	95.34	93.07	106.53	90.90	111.32	96.45	79.38	96.31	122.9
Nd($\times10^{-6}$)	9.59	9.07	11.53	11.34	10.34	9.92	14.09	8.90	8.40	9.03	11.32
Hf($\times10^{-6}$)	2.24	2.32	2.95	2.84	2.55	2.53	2.64	2.27	1.25	2.30	2.86
Zr($\times10^{-6}$)	73.96	75.7	97.65	94.55	88.36	84.47	85.86	75.57	39.33	75.61	107.8
Sm($\times10^{-6}$)	3.38	3.29	4.21	4.06	3.71	3.62	4.49	3.23	3.19	3.32	3.75
Tb($\times10^{-6}$)	0.85	0.85	1.06	1.03	0.95	0.94	1.09	0.83	0.80	0.83	0.87
Y($\times10^{-6}$)	31.87	29.93	39.39	37.58	34.61	34.69	38.27	30.58	29.64	31.56	33.28
Pr($\times10^{-6}$)	1.66	1.60	2.06	1.98	1.85	1.77	2.82	1.56	1.46	1.56	2.25
Eu($\times10^{-6}$)	1.27	1.19	1.48	1.41	1.30	1.28	1.49	1.20	1.17	1.21	1.36
Gd($\times10^{-6}$)	3.63	3.62	4.64	4.48	4.09	4.08	4.92	3.65	3.54	3.71	5.04
Dy($\times10^{-6}$)	5.65	5.9	7.50	7.23	6.22	6.56	7.33	5.84	5.65	5.84	5.78
Ho($\times10^{-6}$)	1.21	1.18	1.5	1.46	1.31	1.34	1.47	1.18	1.13	1.18	1.24
Er($\times10^{-6}$)	3.54	3.38	4.31	4.2	3.97	3.82	4.19	3.32	3.25	3.37	3.6
Tm($\times10^{-6}$)	0.51	0.54	0.69	0.66	0.57	0.59	0.66	0.52	0.51	0.55	0.52
Yb($\times10^{-6}$)	3.30	3.30	4.29	4.06	3.65	3.66	4.04	3.30	3.14	3.35	3.42
Lu($\times10^{-6}$)	0.51	0.52	0.66	0.65	0.57	0.58	0.64	0.52	0.51	0.52	0.51
Pb($\times10^{-6}$)	40.91	0.90	0.62	0.88	2.62	0.58	10.21	0.65	2.60	0.47	0.49
Ta($\times10^{-6}$)	1.04	1.60	0.19	4.71	3.68	0.18	0.18	0.16	1.16	0.16	0.23
Ni($\times10^{-6}$)	128.60	109.18	95.75	101.94	156.3	100.15	91.60	118.87	660.40	155.51	-
Cr($\times10^{-6}$)	282.70	224.73	170.7	198.61	379.8	232.34	199.02	251.42	624.17	316.50	-
Nb/Ta	2.49	2.02	11.70	1.42	1.60	11.10	16.10	9.88	2.29	10.50	14.68

Note: [a]:Niu and O'hara, 2003.

Table 2 Chemical composition of olivine analyzed by electronic microprobe (wt%)

No.	MgO	SiO_2	CaO	MnO	FeO	NiO	Total	Fo	$Mg\#_{(melt)}$	$T_{(liqudus)}$	Rock type
ol-1	39.24	38.58	0.06	0.31	20.51	0.14	98.84	77.32	0.45	1135.71	Olivine -gabbro
ol-2	39.47	37.76	0.08	0.32	20.77	0.14	98.53	77.20	0.45	1134.80	
ol-3	40.59	38.44	0.05	0.35	20.74	0.10	100.27	77.72	0.46	1138.85	
ol-4	39.47	38.99	0.07	0.35	20.70	0.16	99.74	77.27	0.45	1135.26	
ol-5	39.50	37.75	0.07	0.32	20.84	0.14	98.61	77.16	0.45	1134.50	
ol-6	38.68	37.96	0.07	0.36	20.31	0.12	97.50	77.25	0.45	1135.12	
ol-7	39.49	38.01	0.06	0.28	20.17	0.15	98.15	77.73	0.46	1138.92	
ol-8	38.56	38.04	0.06	0.34	22.02	0.11	99.13	75.74	0.42	1124.83	
ol-9	39.87	37.93	0.06	0.32	21.50	0.16	99.84	76.78	0.44	1131.68	
ol-10	38.35	39.67	0.61	0.35	19.61	0.13	98.72	77.71	0.46	1138.75	
ol-11	40.17	40.19	0.05	0.32	21.00	0.17	101.90	77.33	0.45	1135.73	
ol-1	44.26	40.81	0.32	0.23	15.68	0.18	101.48	83.42	0.67	1213.97	Basalt
ol-2	44.06	40.70	0.31	0.22	15.83	0.18	101.30	83.23	0.66	1210.03	
ol-3	42.97	39.13	0.31	0.21	15.50	0.17	98.29	83.18	0.66	1208.94	
ol-4	42.08	39.41	0.31	0.26	15.65	0.16	97.87	82.74	0.64	1200.67	
ol-5	41.26	39.54	0.30	0.20	15.29	0.19	96.78	82.78	0.64	1201.46	
ol-6	42.79	39.73	0.31	0.23	15.88	0.17	99.11	82.77	0.64	1201.22	
ol-7	43.17	40.03	0.29	0.23	15.55	0.19	99.46	83.19	0.66	1209.29	
ol-8	43.18	39.26	0.29	0.26	15.68	0.17	98.84	83.07	0.65	1206.94	

Note: Mg#=atomic ratio Mg*100/(Mg+Fe^{2+}), Fo=atomic ratio Mgol*100/(Mg_{ol}+$Fe^{2+}{}_{ol}$)

Table 3 Chemical composition of clinopyroxene analyzed by electronic microprobe (wt%)

No.	MgO	Al_2O_3	SiO_2	CaO	TiO_2	Cr_2O_3	MnO	FeO	Na_2O	Total	Mg#	Rock type
cpx-1	15.64	2.82	52.75	21.33	1.01	0.13	0.19	6.64	0.33	100.83	80.78	
cpx-2	15.31	2.80	52.51	21.76	1.00	0.13	0.22	6.39	0.39	100.50	81.04	
cpx-3	15.23	2.70	52.22	21.56	1.12	0.12	0.20	6.20	0.39	99.73	81.41	
cpx-4	16.20	2.62	52.27	21.28	1.00	0.15	0.18	6.22	0.38	100.29	82.29	
cpx-5	15.32	2.54	52.84	21.54	0.98	0.15	0.20	6.13	0.33	100.03	81.67	
cpx-6	17.34	2.59	51.79	19.30	1.19	0.12	0.19	7.14	0.37	100.04	81.24	
cpx-7	16.10	2.72	52.15	21.49	1.22	0.15	0.22	6.21	0.37	100.62	82.22	Olivine -gabbro
cpx-8	14.96	2.73	51.65	21.48	1.14	0.13	0.21	6.06	0.45	98.81	81.48	
cpx-9	15.10	3.24	52.40	22.10	1.27	0.16	0.15	6.02	0.42	100.86	81.72	
cpx-10	15.71	3.13	52.55	20.99	1.12	0.12	0.19	6.45	0.45	100.70	81.27	
cpx-11	16.19	3.00	51.61	20.60	1.47	0.13	0.20	6.98	0.33	100.52	80.53	
cpx-12	16.16	2.43	53.83	20.45	0.87	0.12	0.20	6.05	0.43	100.53	82.64	
cpx-13	15.48	2.69	53.17	21.93	1.15	0.11	0.20	6.09	0.37	101.18	81.92	

Note: Mg#=atomic ratio $Mg*100/(Mg+Fe^{2+})$

Table 4 Chemical composition of plagioclase analyzed by electronic microprobe (wt%)

No.	MgO	Al_2O_3	SiO_2	CaO	FeO	Na_2O	Total	An	Rock type
pl-1	0.21	33.77	47.25	17.02	0.35	1.86	100.45	83.53	
pl-2	0.24	32.56	48.00	16.26	0.32	2.18	99.56	80.47	
pl-3	0.18	34.04	48.97	17.08	0.36	1.99	102.61	82.59	
pl-4	0.19	33.98	46.16	17.26	0.28	1.71	99.58	84.79	Basalt
pl-5	0.22	34.84	47.90	17.90	0.29	1.65	102.79	85.73	
pl-6	0.24	34.61	46.99	17.68	0.25	1.68	101.45	85.32	
pl-7	0.22	34.26	47.43	17.38	0.29	1.89	101.47	83.52	
pl-8	0.21	34.26	46.94	17.63	0.30	1.60	100.94	85.90	
pl-1	0.04	31.37	52.02	13.96	0.36	3.85	102.1	66.72	
pl-2	0.06	31.18	52.08	13.63	0.39	4.17	102.31	64.36	
pl-3	0.05	33.66	48.46	16.49	0.39	2.31	101.36	79.75	
pl-4	0.05	31.97	51.28	14.19	0.36	3.67	101.52	68.11	
pl-5	0.05	32.84	49.57	15.52	0.42	2.89	101.29	74.78	
pl-6	0.05	32.95	48.85	15.53	0.38	2.82	100.58	75.29	Olivine
pl-7	0.04	31.70	51.57	13.93	0.41	3.98	101.63	65.94	-gabbro
pl-8	0.04	32.21	49.58	15.01	0.32	3.24	100.40	71.91	
pl-9	0.04	31.99	48.97	15.05	0.39	2.66	99.10	75.77	
pl-10	0.08	32.16	49.96	15.12	0.44	4.24	102.00	66.34	
pl-11	0.07	33.00	49.32	15.80	0.43	3.31	101.93	72.49	
pl-12	0.07	32.14	50.66	14.40	0.40	3.90	101.57	67.12	

Note: An=atomic ratio $CaO/(CaO+Na_2O*2)$

Two groups of plagioclases from the two types of rocks show different ranges of An numbers (Table 4). The An numbers of plagioclase phenocrysts in the basalts range from 80.47 to 85.90 (bytownite series), while plagioclase in the olivine-gabbro shows a relatively low and wide An range: 64.36–79.75 (both labradorite and bytownite series). Furthermore, both groups of plagioclases are K_2O-poor plagioclases. The plagioclase from the olivine-gabbro is characterized by low MgO contents (<0.1 wt%) while the plagioclase from the basalts has slightly higher MgO and FeO contents. Both higher An numbers and the existence of MgO and FeO compositions indicate the relatively primary characteristics of plagioclase phenocrysts in the basalts compared to those of olivine-gabbro.

4.3 Melt inclusion geochemistry and numerical simulation

The composition of parental magma is crucial for studying the post-magma evolution. To obtain the parental magma composition, two approximate approaches can be used: (1) taking the composition of basalts with the lowest degree of differentiation as the relative parental magma composition, providing that all the basalts originated from the same tectonic environment; and (2) looking for melt inclusions within the mineral phenocrysts, as melt inclusions generally represent a lowly evolved magma. In this study, as shown in Table 1, all the basalts are characterized by a

high degree of evolution, even the samples with high MgO (MgO=7.2 wt%). However, as shown in Fig. 2, a multitude of melt inclusions occurred in the plagioclase phenocrysts from basalts. According to their electronic microprobe analysis results, their FeO contents increase with the increase of MgO, and their corresponding Mg# values are generally close to 0.72, which means that that melt evolution had not experienced Ol factional crystallization (Almeev et al., 2008). However, the host mineral-plagioclase phenolcrysts could influence their CaO/Al_2O_3 values, especially Al_2O_3, considering the quite low Al_2O_3 contents and the normal CaO contents. During the simulation, initial value for Al_2O_3 and CaO/Al_2O_3 were chosen in order to fit bulk rock composition on the premise of that it can be taken as a parental magma for within-crust magma differentiation (Niu and O'Hara, 2008), as relative correlations between FeO (CaO, Al_2O_3) and MgO were retained.

In contrast to parental magma, the composition of evolved basalts can be taken as a residual magma which has experienced all the differentiations compared to the parental magma. In terms of their relationship, we can simulate the isobaric magma differentiation processes under different pressures with the COMAGMAT program (Ariskin and Barmina, 2004; Almeev et al., 2008).This can help us establish the relationship between the two magma end-members, thus shedding light on the magma differentiation processes within the crust. In this simulation, we set the magma H_2O content as 0.1 wt% with reference to Almeev et al. (2008), oxygen fugacity to be buffered by the quartz-fayalite-magnetite (QFM) assemblage (Myers and Eugster, 1983), the crystallization increments from 1% up to 60%, and the average modified inclusion composition (only major element oxides) as the starting point. Then, isobaric differentiation crystallization simulations were conducted under the following pressures: 0.1, 1.0, 2.0, 4.0, and 6.0 kbar. Each pressure corresponds to a certain liquid line of descent (LLD) (Almeev et al., 2008), and those LLDs can then be used to determine the effect of pressure on magma evolution.

Two types of simulated LLDs (CaO, Al_2O_3) under different pressures are given in Fig. 5, including the bulk-rock chemistry of parental magma ends and basalts (scattered dots). At all pressures, three stages of magma isobaric partial crystallization can be distinguished: the early stage, middle stage, and late stage. In the early stage (MgO contents are higher than approximately 9.0 wt%), only olivine was separated from the magma, resulting in the increase of CaO and Al_2O_3 contents for the residual magma. The middle stage refers to the olivine-plagioclase co-crystallization stage (MgO contents vary from approximately 9.0 wt% to 8.0 wt%). This stage is characterized by the decrease of CaO and Al_2O_3 contents. The last stage corresponds to the co-crystallization stage of olivine-clinopyroxene-plagioclase (their MgO contents are lower than approximately 8.0 wt%, but different pressures correspond to different initial MgO contents), and is manifested as decreasing CaO contents and increasing Al_2O_3 contents. Given that high pressure is beneficial to the separation of clinopyroxene, for those LLDs, the higher the pressure, the earlier the stage begins (6.0 kbar corresponds to MgO≈8.0 wt%, while 0.1 kbar corresponds to MgO≈6.0 wt%). All the bulk-rock data of basalts appeared in the last stage, in the pressure below 4.0 kbar, based on the depth of magma differentiation H(m) calculation equation (Almeev et al., 2008): $H=(P-\rho_{H_2O}*h_{H_2O})/\rho_{crust}$; where P is pressure (kg/m^2); ρ_{H_2O} is seawater density (1000 kg/m^3), h_{H_2O} is seawater depth, and ρ_{crust} is oceanic crust density (2900 kg/m^3). It was found that the magma differentiation in the region was mainly concentrated at the depth shallower than 13.03 km (4.0 kbar) beneath the seafloor.

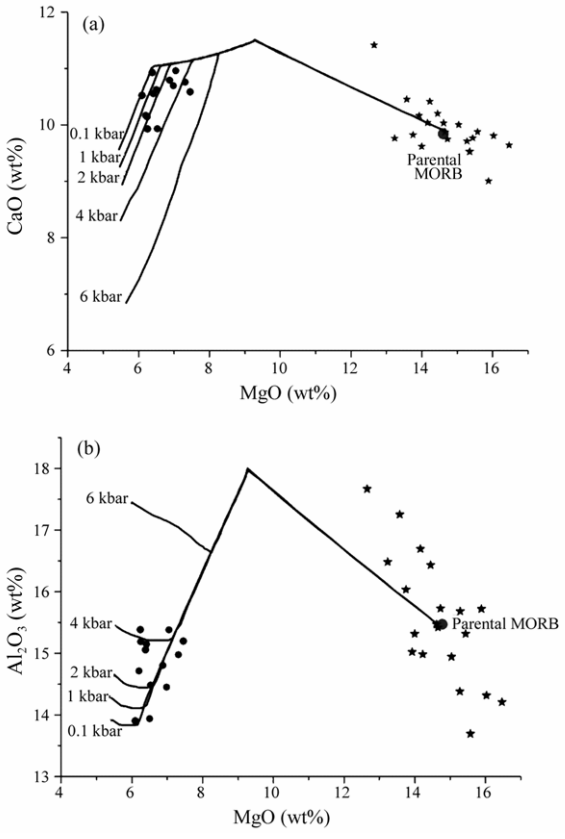

Fig. 5. The simulated LLDs (MgO vs. CaO, Al_2O_3 diagrams) for the parental melt (average modified melt inclusion, red dot in each diagram) at various pressures. Black stars indicate parental magma compositions. Black dots show the evolved magma composition (the bulk content of basalts).

5 Discussion

5.1 Characteristics of magmatic activities in the 14.0°S hydrothermal field

Magma evolution simulation results show that the magmatic differentiation mainly occurred under 4.0 kbar, while no obvious differentiation occurred above 4.0 kbar. The value 4.0 kbar is a distinct pressure boundary, and probably represents the crust-mantle boundary (MOHO) (4.0 kbar corresponds to approximately 13.03 km beneath the seafloor). Beneath this depth, the modified melt inclusions represent parental magma in balance with the mantle (the Mg# of melt inclusions is close to 0.72) (Niu and O'hara, 2008), After the parental magma segregated from the mantle source, it came up into the crust where the dominant magmatic differentiation (partial crystallization) processes occurred; and then rose up rapidly to the seafloor and erupted. This eruption is characterized by a short period of time and a low degree of differentiation.

The magma chamber is the main site where magma differentiation occurs beneath the ridge axis (especially at the fast-spreading ridges) (Singh et al., 2006; Stone and Niu, 2009), but in this region, the vertical differentiation column show distinct differences from the spatial distribution of other magma chambers (Detrick et al., 1987; Calvert, 1995; Singh et al., 2006). The basalt samples, as the magma residuals, show distinctive differences in composition from one another, indicating the weak mixing of magmas in the crust to some extent (Singh et al., 1998; Stone and Niu, 2009). In addition, as an off-axis area, this hydrothermal field is less likely to generate a magma chamber below the seafloor. Instead, there should be a series of magmatic intrusive bodies (Niu and O'hara, 2002; Stone and Niu , 2009) which scattered beneath the seafloor. Magma in some intrusive bodies could occasionally rise up along fractures and erupt onto the seafloor only if induced by tectonics. This type of eruption is of weak intensity and low frequency (Bach and Früh, 2010). Olivine-gabbro (including porphyroclasts in the basalts) represents the differentiation products, showing a low Fo values of olivine, low Mg# , high TiO_2 content of clinopyroxene, and low An number of plagioclase. These features, along with the low MgO contents in the basalts, indicate that magmatic intrusions in the crust experienced durable and relatively thorough differentiation. The high-An numbers of plagioclase porphyroclasts and high-Fo values of olivine porphyroclasts in the basaltic samples are very different from those in the olivine-gabbro, indicating that different magmatic intrusions experienced distinctively different degrees of differentiation. This series of magmatic intrusions generated in the low-degree partial melting zone beneath slowly spreading ridges, after melt extraction, with no obvious mixing with each other, then intruded into the crust in the form of independent magmatic bodies with no stable magma chamber to supply the driving forces of eruption (Niu and O'hara, 2008). The eruption of those magmatic intrusive bodies can only be triggered by appropriate tectonic activities, or alternatively, the heat of magmatic intrusive bodies themselves can be sealed for a long time in the crust. However, if there was a magma chamber beneath the seafloor, there would exist another possibility for the relationship between gabbros and basalts. The basalts containing high-Fo olivine and high-An plagioclase may represent the early erupted, less differentiated magma from the magma chamber beneath the seafloor, whereas the olivine-gabbros may be the result of solidification of the last residual, more evolved magma in the same magma chamber.

5.2 Heat sources within the crust and their effects on the related hydrothermal system

In the absence of a magma chamber, high-temperature thermal anomalies within the crust are mainly derived from the magma intrusions and their associated crystallized rock bodies (Stone et al., 2009). Given that the 14.0°S hydrothermal field is located in the off-axis region, most of the intrusive bodies have crystallized and cooled to normal temperatures, but several crystallized high-temperature rock bodies should exist within the near-axis crust (Fig. 6). According to our olivine geochemistry studies (Section 4.2) which reflected a high (＞1100℃) mineral crystallization temperature, abundant heat was stored in the near-axis crystallized rock bodies, which therefore were likely to act as potential high-temperature thermal anomalies. In the off-axis area, with intenfiying magmatism, tectonic activities increase, providing convenient pathways (a large number of tectonic fractures) for seawater to penetrate downwards until it reaches the high-temperature rock bodies (Mccaig, 2010); the seawater then mines heat energy of the hot rocks. Because of the solidity and small scale of the rock bodies, during their interaction with seawater, no conductive boundary layer developed in the reaction zone similar to that of a steady-state magma chamber (Alt, 1995). Instead, the reaction zone is characterized by a "cracking front" (Alt, 1995; Wilcock and Delaney, 1996) resulting from thermal contraction. The "cracking front" in turn led to the increase of contact area between seawater and hot rocks. A large quantity of penetrated seawater was therefore heated to high temperature, then the heated seawater leached the surrounding rocks and was pushed upwards rapidly by buoyancy forces until

it reached the other upper-crust seafloor to form the mineralization system (Tivey, 2007; Coumou et al., 2008). The development of a "cracking front", together with off-axis tectonic activities, led to elevated crust permeability. Furthermore, as discussed in previous studies (Alt, 1995; Wilcock and Delaney, 1996; Lowell, 2010), the continuous development of a "cracking front" was able to provide persistent heat-flow for the hydrothermal system.

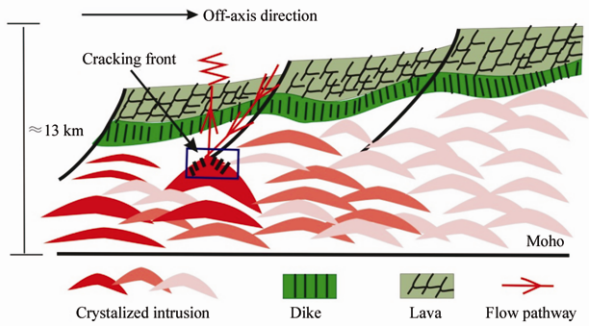

Fig. 6. Sketch illustrating the inferred crystallized intrusions and related hydrothermal system within the off-axis crust. For the crystallized intrusions, the deeper the color, the higher the temperature.

6 Conclusions

(1) Bulk-rock major and trace elements compositions of the basalts from the 14.0°S hydrothermal field indicate that the basalts there are typical N-MORB. Both the primitive mantle-normalized trace elements spider diagram and the chondrite-normalized REE (rare-earth elements) patterns exhibit typical "left-leaning" distribution patterns. These two features, together with the low MgO contents and high SiO_2 contents of the basalts, suggest that the magma experienced strong differentiation in the crust. Nb/Ta ratios in the basalts are significantly lower than those in the average N-MORB, indicating that the clinopyroxene has crystallized under high pressure conditions in this area.

(2) Geochemical studies of minerals (magma segregation within the crust) in the olivine-gabbro illustrate strong magma differentiation (low-Fo olivine, low-Mg# clinopyroxene, high-TiO_2 clinopyroxene, low-An plagioclase) within the crust as well. Nevertheless, these mineralogical characteristics are significantly different from those of mineral phenocrysts in the basalts (high-Fo olivine, high-An plagioclase), reflecting the heterogeneity of magma differentiation within the crust. However, if there was a magma chamber beneath the seafloor, the basalts containing high-Fo olivine and high-An plagioclase may represent the early erupted, less differentiated magma from the magma chamber beneath the seafloor, whereas the olivine-gabbro may be the result of solidification of the residual, more evolved magma in the same magma chamber.

(3) Through mineral geochemistry and numerical simulation of isobaric differentiation for magma evolution, magmatic differentiation within the crust was suggested to have occurred within a 13.03 km thick crust. The vertical differentiation column shows distinct differences compared to the spatial distribution of steady-state magma chambers. This inconsistence with magma chambers, in combination with the heterogeneity of magma differentiation within the crust, suggests a high likelihood of the development of a series of independent magma intrusions within the crust rather than in a steady-state magma chamber.

(4) As the primary high-temperature thermal anomalies within the off-axis crust, crystallized intrusions are the most probable heat sources for the 14.0°S hydrothermal system. The penetrated seawater constantly mines heat energy of crystallized intrusions through a gradually widening "cracking front," which in turn leads to the increase of contact area between seawater and hot rocks. The development of a "cracking front", together with off-axis tectonic activities, lead to the elevation of crust permeability. Therefore, the development of high-temperature crystallized magma intrusions plays a key role in the 14.0°S hydrothermal system.

Acknowledgements This research project was financially supported jointly by the China Ocean Mineral Resources Research and Development Association Program (DY125-12-R-01) and the National Natural Science Foundation of China (NSFC41306060). Great thanks are due to all the crew and scientists of the RV "DayangYihao" Cruises 21 and 22.

References

Almeev R., Holtz F., Koepke J., Haase K., and Devey C. (2008) Depths of partial crystallization of H_2O-bearing MORB: Phase equilibria simulations of basalts at the MAR near Ascension Island (7°–11°S) [J]. *Journal of Petrology*. **49**, 25–45.

Ariskin A.A. and Barmina G.S. (2004) COMAGMAT: Development of a magma crystallization model and its petrological applications [J]. *Geochemistry International*. **42**, 1–157.

Bach W. and Früh-Green G.L. (2010) Alteration of the oceanic lithosphere and implications for seafloor processes [J]. *Elements*. **6**, 173–178.

Baker E.T. (2009) Relationships between hydrothermal activity and axial magma chamber distribution, depth, and melt content [J]. *Geochemistry, Geophysics, Geosystems*. **10**, 1–15.

Calvert A. (1995) Seismic evidence for a magma chamber beneath the slow-spreading Mid-Atlantic Ridge [J]. *Nature*. **377**, 410–414.

Chen Y.J. and Lin J. (1999) Mechanisms for the formation of ridge-axis topography at slow-spreading ridges: A lithospheric-plate flexural model [J]. *Geophysics Journal International*. **136**, 8–18.

Coumou D., Driesner T., and Heinrich C.A. (2008) The structure and dynamics of mid-ocean ridge hydrothermal systems [J]. *Science*. **321**, 1825–1828.

Dekov V., Boycheva T., Hålenius U., Billström K., Kamenov G.D., Shanks W.C., and Stummeyer J. (2011) Mineralogical and geochemical evidence for hydrothermal activity at the west wall of 12°50′N core complex (Mid-Atlantic Ridge): A new ultramafic-hosted seafloor hydrothermal deposit [J]. *Marine Geology*. **288**, 90–102.

Detrick R., Buhl P., Vera E., Mutter J., Orcutt J., Madsen J., and Brocher T. (1987) Multi-channel seismic imaging of a crustal magma chamber along the East Pacific Rise [J]. *Nature*. **326**, 35–41.

Devey C.W., German C., Haase K., Lackschewitz K., Melchert B., and Connelly D. (2010) *The Relationships Between Volcanism, Tectonism, and Hydrothermal Activity on the Southern Equatorial Mid-Atlantic Ridge* [M]. pp.133–152. Geophysical Monograph Series.

Dick H.J.B., Lin J., and Schouten H. (2003) An ultraslow-spreading class of ocean ridge [J]. *Nature*. **426**, 405–412.

Fouquet Y. (1997) Where are the large hydrothermal sulphide deposits in the oceans [J]. *Philosophical Transactions of the Royal Society A: Mathematical, Physical and Engineering Sciences.* **355**, 427–441.

German C.R. and Lin J. (2004) *The Thermal Structure of The Oceanic Crust, Ridge-Spreading and Hydrothermal Circulation: How Well do We Understand Their Inter-Connections* [M]. Mid-Ocean Ridges: Hydrothermal Interactions Between the Lithosphere and Oceans, Geophys. Monogr. Ser. **148**, 1–18.

Haase K., Koschinsky A., Petersen S., Devey C.W., German C., Lackschewitz K.S., Melchert B., Seifert R., Borowski C., and Giere O. (2009) Diking, young volcanism and diffuse hydrothermal activity on the southern Mid-Atlantic Ridge: The Lilliput field at 9°33′S [J]. *Marine Geology*. **266**, 52–64.

Hannington M.D., Ronde de C.E.J., and Petersen S. (2005) *Sea-Floor Tectonics and Submarine Hydro-Thermal Systems* (eds. Hedenquist J. et al.) [M]. pp.111–141. 100th Anniversary Volume of Economic Geology. Society of Economic Geologists, Littleton, Colorado.

Kelley D.S. and Karson J.A. (2001) An off-axis hydrothermal vent field near the Mid-Atlantic Ridge at 30N [J]. *Nature.* **412**, 145–149.

Lowell R.P. (2010) *Hydrothermal Circulation at Slow Spreading Ridges: Analysis of Heat Sources and Heat Transfer Processes* [M]. pp.11–26. Geophysical Monograph Series.

Macdonald K.C., Scheirer D.S., and Carbotte S.M. (1991) Mid-ocean ridges: Discontinuities, segments and giant cracks [J]. *Science*. **253**, 986.

Mccaig A.M., Delacour A., Fallick A.E., Castelain T., and Fruh-Green G.L. (2010) *Detachment Fault Control on Hydrothermal Circulation Systems: Interpreting the Subsurface Beneath the Tag Hydrothermal Field Using the Isotopic and Geological Evolution of Oceanic Core Complexes in the Atlantic* [M]. pp.207–240. Diversity of Hydrothermal Systems on Slow Spreading Ocean Ridges, Geophys. Monogr. Ser.

Mccaig A.M. and Harris M. (2012) Hydrothermal circulation and the dike-gabbro transition in the detachment mode of slow seafloor spreading [J]. *Geology.* **40**, 367–370.

Morimoto N. (1988) Nomenclature of pyroxenes [J]. *Mineralogy and Petrology*. **39**, 55–76.

Myers J.T. and Eugster H. (1983) The system Fe-Si-O: Oxygen buffer calibrations to 1500 K [J]. *Contributions to Mineralogy and Petrology*. **82**, 75–90.

Niu Yaoling and O'hara M.J. (2003) Origin of ocean island basalts: A new perspective from petrology, geochemistry, and mineral physics considerations [J]. *Journal of Geophysical Research: Solid Earth*. **108**, 2209–2213.

Niu Yaoling and O'hara M.J. (2008) Global correlations of ocean ridge basalt chemistry with axial depth: A new perspective [J]. *Journal of Petrology*. **49**, 633–664.

Presnall D. and Hoover J. (1987) High pressure phase equilibrium constraints on the origin of mid-ocean ridge basalts in magmatic processes: Physicochemical principles. In G*eochemistry Society Publication* (special paper) [C]. **1**, 75–89.

Roeder P. and Emslie R. (1970) Olivine-liquid equilibrium [J]. *Contributions to Mineralogy and Petrology*. **29**, 275–289.

Singh S.C., Kent G., Collier J., Harding A., and Orcutt J. (1998) Melt to mush variations in crustal magma properties along the ridge crest at the southern East Pacific Rise [J]. *Nature*. **394**, 874–878.

Singh S.C., Crawford W.C., Carton H., Seher T., Combier V., Cannat M., Canales J.P., Düsünür D., Escartin J., and Miranda J.M. (2006) Discovery of a magma chamber and faults beneath a Mid-Atlantic Ridge hydrothermal field [J]. *Nature*. **442**, 1029–1032.

Stone S. and Niu Yaoling (2009) Origin of compositional trends in clinopyroxene of oceanic gabbros and gabbroic rocks: A case study using data from ODP Hole 735B [J]. *Journal of Volcanology and Geothermal Research*. **184**, 313–322.

Tao Chunhui, Li Huaiming, Yang Yaomin, Ni Jianyu, Cui Ruyong, Chen Yongshun, He Yonghua, Li Jiaobiao, Huang Wei, Lei Jijiang., and Wang Yejian (2011) Two hydrothermal fields found on the Southern Mid-Atlantic Ridge [J]. *Science China—Earth Sciences*. **41**, 887–889.

Tivey M.K. (2007) Generation of seafloor hydrothermal vent fluids and associated mineral deposits [J]. *Oceanography.* **20**, 50–65.

Tucholke B.E. and Lin J. (1994) A geological model for the structure of ridge segments in slow spreading ocean crust [J]. *Journal of Geophysical Research*. **99**, 11937–11958.

Von Damm K.L. (2001) Lost city found [J]. *Nature*. **412**, 127–128.

Wilcock W.S.D. and Delaney J.R. (1996) Mid-ocean ridge sulfide deposits: Evidence for heat extraction from magma chambers or cracking fronts [J]. *Earth and Planetary Science Letters*. **145**, 49–64.

Wilcock W.S.D., Hooft E.E., Toomey D.R., McGill P.R., Barclay A.H., Stakes D.S., and Ramirez T.M. (2009) The role of magma injection in localizing black-smoker activity [J]. *Nature Geoscience*. **2**, 509–513.